

Space Weather®

L

RESEARCH ARTICLE

10.1029/2022SW003073

Key Points:

- Daily eastward dynamo electric fields in the equatorial ionosphere are derived by the distance of equatorial ionization anomaly (EIA) crests in global ionosphere maps
- The derived dynamo electric fields are used as input to ionosphere models to have a better understanding on the space weather
- The distance of EIA crests minimizes the trans-equatorial wind effects in the estimation of daily dynamo electric fields

Correspondence to:

J.-Y. Liu, tigerjyliu@gmail.com

Citation:

Cheng, C.-C., Liu, J.-Y., Lin, C. C. H., & Cheng, Y.-C. (2022). Daily dynamo electric fields derived by using equatorial ionization anomaly crests of the total electron content. *Space Weather*, 20, e2022SW003073. https://doi.org/10.1029/2022SW003073

Received 23 FEB 2022 Accepted 15 OCT 2022

Author Contributions:

Conceptualization: Jann-Yenq Liu Data curation: Ching-Chung Cheng Formal analysis: Ching-Chung Cheng, Yin-Chen Cheng

Funding acquisition: Jann-Yenq Liu **Investigation:** Ching-Chung Cheng, Jann-Yenq Liu, Charles C. H. Lin

Methodology: Ching-Chung Cheng, Jann-Yenq Liu Software: Ching-Chung Cheng,

Yin-Chen Cheng
Validation: Jann-Yeng Liu, Charles

Validation: Jann-Yenq Liu, Charles C. H. Lin

Writing – original draft: Ching-Chung Cheng, Jann-Yenq Liu Writing – review & editing: Ching-

Chung Cheng, Jann-Yenq Liu, Charles C. H. Lin

© 2022. The Authors.

This is an open access article under the terms of the Creative Commons Attribution License, which permits use, distribution and reproduction in any medium, provided the original work is properly cited.

Daily Dynamo Electric Fields Derived by Using Equatorial Ionization Anomaly Crests of the Total Electron Content

Ching-Chung Cheng¹, Jann-Yenq Liu^{1,2,3}, Charles C. H. Lin⁴, and Yin-Chen Cheng⁴

¹Department of Space Science and Engineering, National Central University, Taoyuan, Taiwan, ²Center for Astronautical Physics and Engineering, National Central University, Taoyuan, Taiwan, ³Center for Space and Remote Sensing Research, National Central University, Taoyuan, Taiwan, ⁴Department of Earth Sciences, National Cheng Kung University, Tainan, Taiwan

Abstract Latitudinal distances between the two equatorial ionization anomaly (EIA) crests in total electron content (TEC) of global ionosphere map (GIM) are used to derive the daily dynamo eastward electric field by comparing the eastward electric field calculated by ROCSAT-1 vertical ion velocity in four seasons. The electric fields derived by the EIA crests of GIM TEC, ROCSAT-1 ion velocity, and the incoherent scatter radar (ISR) observations at Jicamarca are generally in good agreement in longitudes and seasons. Meanwhile, the electric fields derived by the EIA crests agree well with those by ROCSAT-1, FORMOSAT-7/COSMIC-2, and Jicamarca ISR on individual days. A long-term study of the GIM-TEC crest distance reveals obvious solar activity dependency of the daily dynamo electric field during 1999–2020. These agreements confirm that the EIA crest can be used to derive the daily eastward dynamo electric field and the associated vertical ion velocity which is responsible to the strength of equatorial plasma fountain and the latitudinal extend of the EIA. Moreover, the vertical ion velocity derived by the GIM-TEC crest distance is further used to improve the SAMI2 model for space weather applications.

Plain Language Summary Equatorial ionization anomaly (EIA) is the most prominent feature in the ionosphere. During the morning, the eastward electric field induced by the tidal wind in the off-equator E-region activates the E × B plasma fountain and results in the prominent EIA crests on both sides of the magnetic equator. The global ionosphere map (GIM) routinely and globally displays the EIA crest of total electron content (TEC). Here, we show that the latitudinal distance of the GIM TEC crests between northern and southern hemispheres can be used to derive the daily eastward dynamo electric field and the associated vertical ion velocity in the equatorial ionosphere. Moreover, the derived vertical ion velocity is further used to improve ionosphere models for space weather applications.

1. Introduction

Equatorial ionization anomaly (EIA) is the most prominent feature in the ionosphere (Davies, 1990; Kelley, 2009; Ratcliffe, 1974). During the morning, the eastward electric field induced by the tidal wind in the off-equator E-region is mapped along magnetic field lines into the equatorial F-region, which activates the $E \times B$ fountain and uplifts the plasma to the upper F-region. Owing to the gravity and plasma pressure gradients, the plasma further preferentially diffuses along the magnetic field and leads to the prominent EIA crests on both sides of the magnetic equator (Anderson, 1973; Anderson et al., 2002; Duncan, 1960; Hanson & Moffett, 1966; Ratcliffe, 1974; Wright, 1963). It is well known that ionospheric weather, especially over the EIA region, strongly affects Global Navigation Satellite System (Klobuchar, 1991; Yue et al., 2016), satellite-based navigation (Roy and Paul, 2013), and high-frequency (HF) radar communication (Freeman, 2006; Harris, 2005; Yeh et al., 1972). $E \times B$ drifts driving the equatorial plasma fountain play an important role on the formation of large-scale ionospheric features such as wavenumber-4 (Sagawa et al., 2005; Immel et al., 2006) and equatorial irregularities (Dabas et al., 2003; Fejer et al., 1999), which significantly influence satellite and HF radar communications. A better understanding on the $E \times B$ drifts is essential to clarify the mechanism of those ionospheric features which are of value for navigation and communication systems.

Rastogi and Klobuchar (1990) reported that the latitudinal locations of the EIA crests of the total electron content (TEC) are dependent on the strength of the equatorial electrojet (EEJ) current which can be estimated by the deviation in the horizontal H component (Δ H). Chen et al. (2008) find that latitudinal locations of the EIA crests

CHENG ET AL. 1 of 10

of TEC are proportional to ΔH , and the time delay of about 3–4 hr between EIA crest and ΔH maximum is a function of seasons. Anderson et al. (2004) observed the significant correlation between ΔH and vertical $E \times B$ drifts in the Peruvian longitude sector, while Fang et al. (2008) utilize TIE-GCM model simulations to find the relationship between ΔH and vertical $E \times B$ drifts. Fang et al. (2009) compare Global Ionosphere Plasmasphere model simulations and ROCSAT-1 observations and report the causal link between EIA crests and vertical $E \times B$ drifts.

Scherliess and Fejer (1999) employed Jicamarca plasma drift from 1968 to April 1992 and Atmosphere Explorer satellite vertical plasma drifts from January 1977 to December 1979 to establish an empirical equatorial vertical drift model. Fejer et al. (2008) utilizing ROCSAT-1 observations in 1999-2004 constructed a quiet time global empirical model for vertical plasma drifts in the equatorial F region. The two models have been widely used as input for most of the general ionospheric models such as SUPIM (Sheffield University Plasmasphere Ionosphere Model) (e.g., Bailey & Balan, 1996; Bailey et al., 1997; Bravo et al., 2017, 2019) and SAMI-2/SAMI-3 (SAMI2 is another model of the Ionosphere) (Chen et al., 2013; Huba et al., 2000). To extend databases of the two models, EIA crest locations in the global ionosphere map (GIM) of TEC are employed to derive the daily eastward dynamo electric field, while ROCSAT-1 vertical ion velocities are utilized to compute the co-located and concurrent zonal electric field (Kelley, 2009). Based on the correlation between the EIA crest location of GIM-TEC and the computed zonal electric field in the same magnetic longitude during the morning period of 1999–2004, we study the daily eastward dynamo electric field using the distances of EIA crest of the GIM-TEC in the equatorial ionosphere at various local time, longitudes, seasons, and solar activities. The developed GIM-TEC technique allows us studying daily dynamo eastward electric fields from 2005 to 2020, which can be not only applied to derive daily dynamo electric fields as a stand-alone model in the equatorial ionosphere, but also used to be the $E \times B$ drift input of existing global ionosphere models.

2. Methodology and Observations

To find the correlation between the EIA crest location and the equatorial eastward electric field, we examine EIA crest locations of GIM-TEC routinely published by Center for Orbit Determination in Europe (CODE) every 2 hr with the 2.5° geographic latitude $\times 5^{\circ}$ geographic longitude spatial resolution, and vertical ion drifts measured by ROCSAT-1 (Chang et al., 1999; Su et al., 1999; Yeh et al., 1999) with an inclination of 35° during 1999–2004. Based on Kelley (2009), the upward ion velocity, $V_{\rm Z}$, can be used to derive the associated eastward electric field, $E_{\rm X}$, which can be expressed as,

$$E_{\mathbf{X}}\,\hat{\mathbf{z}} = -V_{\mathbf{z}}\,\hat{\mathbf{z}} \times B_{\mathbf{y}}\,\hat{\mathbf{y}},\tag{1}$$

where $B_{\rm Y}$ is the northward component of Earth's magnetic field from IGRF (International Geomagnetic Reference Field, http://wdc.kugi.kyoto-u.ac.jp/igrf/index.html). From Equation 1, we use the observed ROCSAT-1 ion upward velocity ($V_{\rm Z~ROC}$) to estimate the eastward electric field $E_{\rm X~ROC}$ within $\pm 9^{\circ}$ magnetic latitudes.

Figure 1 depicts a typical GIM at 1900 UT on 21 September 2001, which reveals two EIA crest latitudes, the northern (L_n) and southern (L_s) , together with their distance of the two $(\Delta L = L_n - L_s)$ in TEC appearing between -135 and -30° E longitude during 1000–1700 local time. We further focus on the geomagnetic quiet condition of Dst ≥ -30 nT, and statistically analyze the correlation between E_{X_ROC} and $L_n/L_s/\Delta L$ in 4 seasons of M-month (February–April), J-month (May–July), S-month (August–October), and D-month (November–January) during 1999–2004. Following Chen et al. (2008), we take into consideration of that E_X leads $L_n/L_s/\Delta L$ by 4 hr in M-and S-month and 3 hr in J- and D-month, and compute the correlation coefficients accordingly. For example, in S-month, once $L_n/L_s/\Delta L$ is defined, we find the col-located E_X 4 hr earlier. To remove unwanted background noises, we further calculate the median of E_{X_ROC} , which is denoted \tilde{E}_{X_ROC} , and its associated $L_n/L_s/\Delta L$. Figure 2 shows that for the 95% confidence interval, the correlation coefficients of \tilde{E}_{X_ROC} versus L_n , L_s , and ΔL are significant in the four seasons. The positive and negative correlation coefficients indicate that the EIA crests move poleward in the northern and southern hemispheres, which is associated larger eastward electric fields. Similarly, the larger ΔL should result from the stronger eastward electric field. Note that the correlation coefficient of \tilde{E}_{X_ROC} - ΔL is systematically greater than that of \tilde{E}_{X_ROC} -L L or \tilde{E}_{X_ROC} -L L in each month. This suggests that the trans-equatorial neutral wind is essential, and ΔL is a better parameter to estimate the eastward electric field.

Based on the slope of m and the intercept on the y-axis of s in Figure 2, the equatorial eastward electric field $E_{X_\Delta L}$ can be expressed as,

CHENG ET AL. 2 of 10

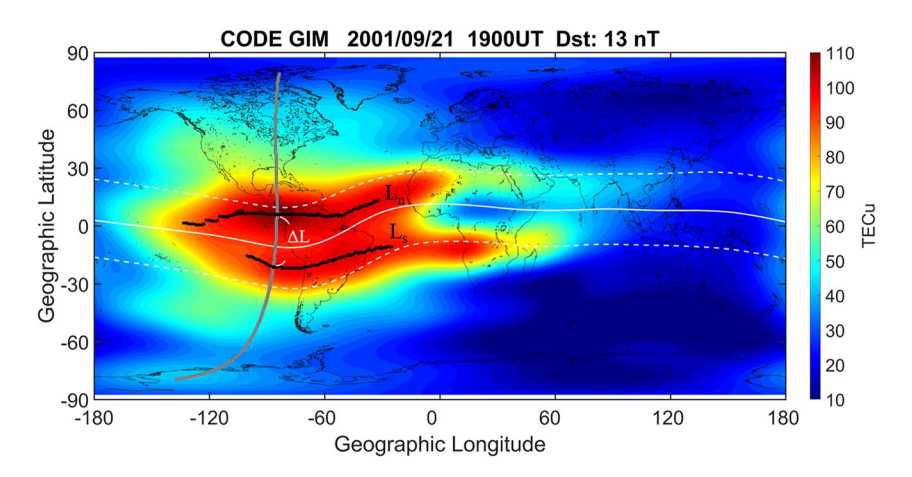


Figure 1. The typical Center for Orbit Determination in Europe global ionosphere map at 1900°UT on 21 September 2001. Black dots indicate equatorial ionization anomaly crest positions. The white solid line represents the magnetic equator, the white dashed lines are $\pm 20^{\circ}\text{N}$ magnetic latitude, and the gray solid line stands for a magnetic flux tube at -13.6°E magnetic longitude.

$$E_{X,\Delta L} = \frac{\Delta L - s}{m}.$$
 (2)

Thus, ΔL along each longitude can be used to derive $E_{\rm X, \Delta L}$ in various longitudes and seasons during the 5 years of 1999–2004. The approach consists of the following steps:

- Step 1. Find the magnetic latitude of north and south EIA crest locations along the same magnetic longitude.
- **Step 2.** Compute the latitudinal distance (i.e., ΔL) of the two EIA crests.
- **Step 3.** Derive $E_{X_{\Delta}L}$ via Equation 2 and the associated $E \times B$ drift (i.e., $V_{Z_{\Delta}L}$) via Equation 1.

Meanwhile, Fejer et al. (2008) used 5-year ROCSAT-1/IPEI measurements in 1999–2004 constructing a quiet time global empirical model for vertical plasma drifts in the equatorial F region. Following Fejer et al. (2008) and based on Equation 1, we compute the diurnal variations of the upward ion velocity, $V_{\rm Z_ROC}$, and derive the associated eastward electric field, $E_{\rm X_ROC}$, at the magnetic equator in various longitudes and seasons during the study period. Figure 3 reveals that in general, the pattern of $E_{\rm X_AL}$ agrees well with that of $E_{\rm X_ROC}$, where the two electric fields begin increasing in the morning around 0600 LT, reach their maximum at 1000-1200 LT, and subsequently decrease after 1200 LT. Table 1 lists the root-mean-square errors (RMSEs) between $E_{\rm X_AL}$ and $E_{\rm X_ROC}$.

For overall (-180 to 180° longitude), $E_{\rm X_\Delta L}$ is nearly identical to $E_{\rm X_ROC}$, especially in M-, J-, and S-months (RMSEs = 0.05–0.12 mV/m). This shows that ΔL in GIM TEC can be used to estimate the eastward electric field at the magnetic equator in various longitudes from 0400–0600 to 1200–1400 LT. We further utilize electric fields observed by the incoherent scatter radar at Jicamarca Radio Observatory (-11.95° N, -76.87° E, 1° N, magnetic), $E_{\rm X_JRO}$, to validate $E_{\rm X_\Delta L}$. Table 1 also displays the RMSEs between $E_{\rm X_\Delta L}$ and $E_{\rm X_JRO}$. Figure 3 and Table 1 depict that $E_{\rm X_\Delta L}$ and $E_{\rm X_ROC}$ well agree with $E_{\rm X_JRO}$, especially in M-, S-, and D-month (RMSEs = 0.10–0.18 mV/m). However, in J-month, $E_{\rm X_AL}$ has been somewhat underestimated at 0530–0600 LT, but overestimated at 0700–1230 LT, while $E_{\rm X_JRO}$ is slightly larger than $E_{\rm X_ROC}$ during 0400–0600 LT. Nevertheless, overall, the strength and variation of $E_{\rm X_AL}$ are compatible, and yield a similar tendency to those of $E_{\rm X_ROC}$ and $E_{\rm X_JRO}$ in each longitude, especially during equinoxes.

Since $E_{\rm X_AL}$, $E_{\rm X_ROC}$, and $E_{\rm X_JRO}$ in various longitudes and seasons generally yield nearly identical tendencies, we then try to derive $E_{\rm X_AL}$ at Jicamarca on a certain day. Figure 4 displays the diurnal variation of GIM TEC as well as the eastward electric fields of $E_{\rm X_AL}$, $E_{\rm X_JRO}$, and $E_{\rm X_ROC}$ on 19 March 2002 (solar radio flux at 10.7 cm, F10.7 = 173.3 sfu, solar flux unit). $E_{\rm X_AL}$ begins to elevate in 0900–1100 LT and yield a constant value in 1100–1230 LT, which is almost the same as $E_{\rm X_JRO}$ (RMSE = 0.17 mV/m). On the other hand, $E_{\rm X_ROC}$ has a constant value in 0900–1200 LT and begins to decline after 1200 LT (RMSE = 0.21 mV/m). Nevertheless, general patterns and values among the three electric fields are nearly identical during 0900–1300 LT. We further calculate the eastward electric field, $E_{\rm X_F7C2}$, by FORMOSAT-7/COSMIC-2 upward ion velocity, and derive the

CHENG ET AL. 3 of 10

elibrary.wiley.com/doi/10.1029/2022SW003073 by University Of Colorado Librari, Wiley Online Library on [01/08/2023]. See the Terms

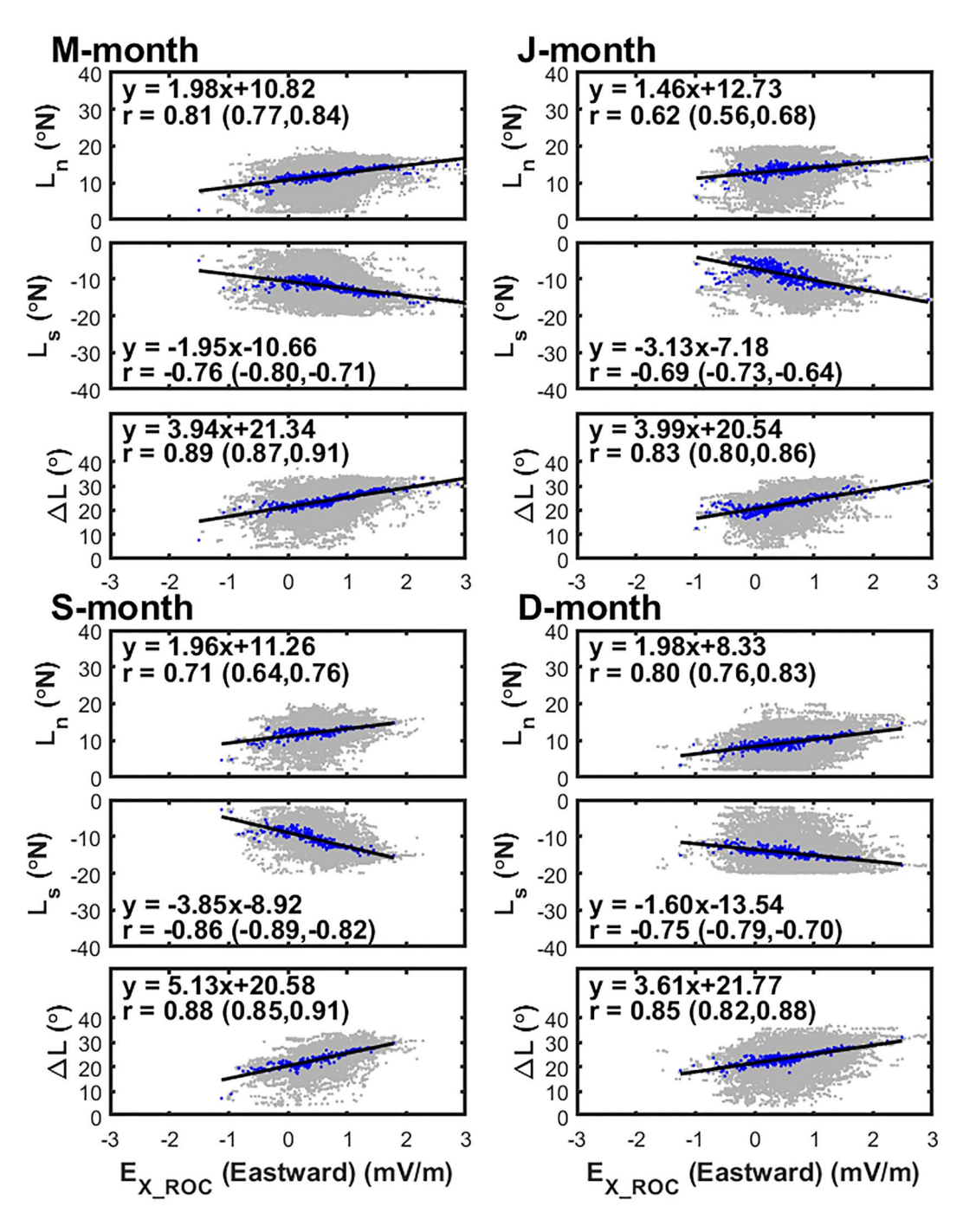


Figure 2. Scatterplots of E_{X_ROC} versus $L_n/L_s/\Delta L$ in various seasons of 1999–2004. Gray dots are E_{X_ROC} and its associated $L_n/L_s/\Delta L$. Blue dots are the median of 100-points of E_{X_ROC} , \tilde{E}_{X_ROC} , sorted from smallest to largest one and its associated $L_n/L_s/\Delta L$. Black solid lines represent the linear regression of the blue dots. Correlation coefficients and linear regression equations of the blue dots are denoted in each figure. The parenthesis behind the correlation coefficients is the associated 95% confidence interval.

collocated/concurrent $E_{\rm X_\Delta L}$ at $-120^{\circ}{\rm E}$ longitude on 25 September 2019 (F10.7 = 67.9 sfu). Figure 5 shows that the tendency of $E_{\rm X_\Delta L}$ is very similar to $E_{\rm X_ROC}$ (RMSE = 0.24 mV/m), while $E_{\rm X_F7C2}$ tends to decrease in 0700–1230 LT (RMSE = 0.19 mV/m). Nonetheless, the general pattern of $E_{\rm X_\Delta L}$ is comparable with $E_{\rm X_F7C2}$ and $E_{\rm X_ROC}$ during 0630–1230 LT. The almost identical patterns between $E_{\rm X_\Delta L}$ and $E_{\rm X_ROC}/E_{\rm X_ROC}/E_{\rm X_F7C2}$ (Figures 4

CHENG ET AL. 4 of 10

15427390, 2022, 11, Downloaded from https://agupubs.onlinelibrary.wiley.com/doi/10.1029/2022SW003073 by University Of Colorado Librari, Wiley Online Library on [01/8/2023]. See the Terms

ditions) on Wiley Online Library for rules of use; OA articles are governed by the applicable Creati

0.27

0.46

0.25

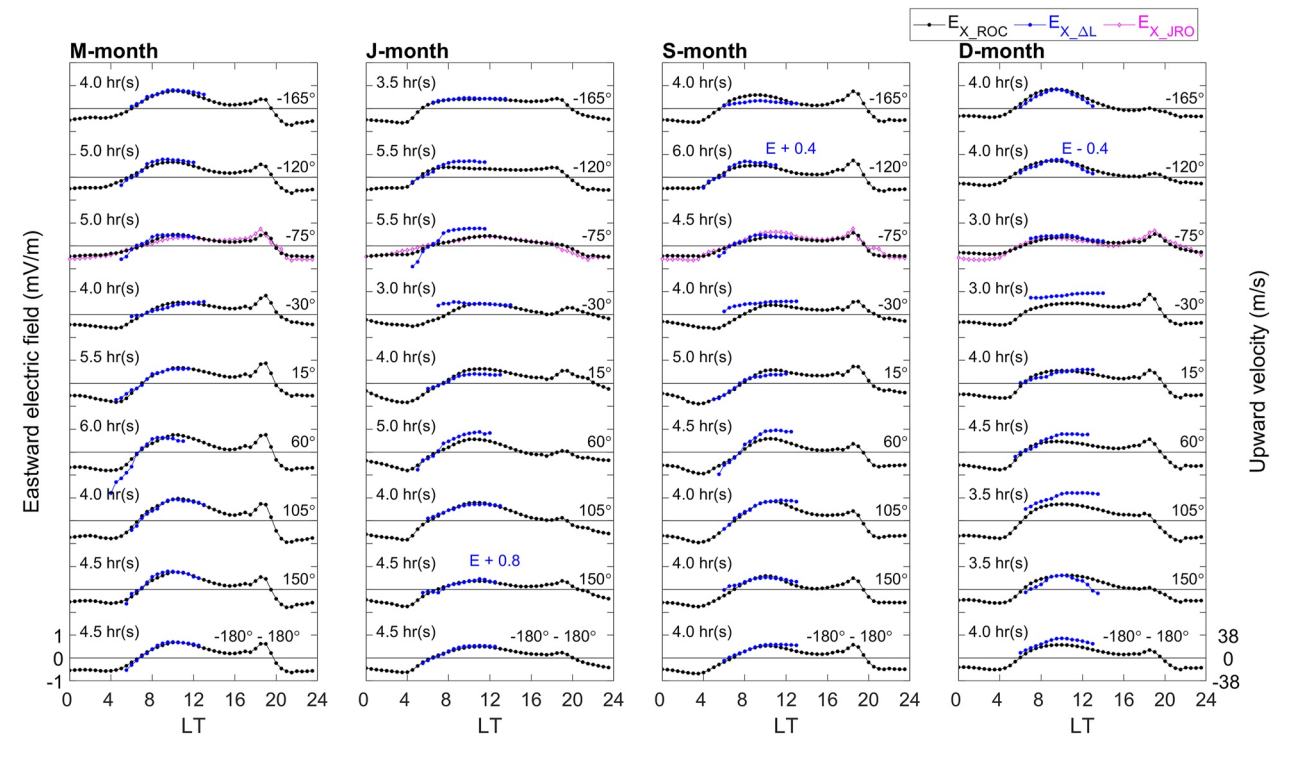


Figure 3. Diurnal variations of $E_{X_\Delta L}$ and E_{X_ROC} in various seasons and longitudes. Due to the offset between $E_{X_\Delta L}$ and E_{X_ROC} , the time leading of 3–6 hr denoted in the figure is determined by root mean square errors between $E_{X_\Delta L}$ and E_{X_ROC} . The magenta lines are E_{X_ROC} derived from vertical ion drifts in 300–400 km altitude at Jicamarca. E_{X_ROC} is the eastward electric field derived by the ROCSAT-1 upward ion velocity within $\pm 9^{\circ}$ N magnetic latitude every 30 min.

and 5) indicates that GIM-TEC Δ L can be used to be a proxy of the diurnal variation of the eastward electric field on an individual day during both high and low solar activities. Owing to the agreements in Figures 3–5, we further apply Δ L of the GIM-TEC crests examining the equatorial eastward electric field of the globe during the long-term period of 1999–2020. Figure 6 illustrates $E_{\rm X_\Delta L}$ at 1100 LT in various longitudes and the associated longitudinal averages as well as F10.7 during the study period, which shows that variations of the global averaged $E_{\rm X_\Delta L}$ and the solar activity yield similar tendencies.

Table 1Root-Mean-Square Errors Between $E_{X_\Delta L}$ and E_{X_ROC}				
RMSE (mV/m)	M-month	J-month	S-month	D-month
-165°	0.08	0.04	0.20	0.13
−120°	0.13	0.22	0.12	0.10
−75°	0.13 (0.18, 0.07)	0.37 (0.42, 0.10)	0.11 (0.14, 0.12)	0.10 (0.12, 0.10)
−30°	0.11	0.26	0.36	0.44
15°	0.09	0.16	0.12	0.13

0.24

0.06

0.08

0.30

0.13

0.13

 $-180^{\circ}-180^{\circ}$ 0.07 0.05 0.12 0.23 Note. Numbers in the bracket denote root-mean-square errors between (former) $E_{\rm X_\Delta L}$ and $E_{\rm X_JRO}$ as well as (latter) $E_{\rm X_\Delta L}$ and $E_{\rm X_JRO}$ as well as (latter) $E_{\rm X_AL}$

CHENG ET AL. 5 of 10

0.36

0.08

0.10

60°

105°

150°

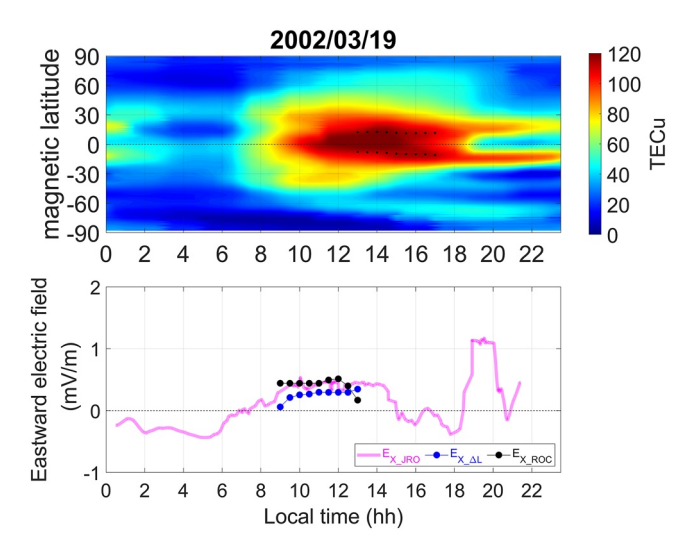


Figure 4. The diurnal variation of global ionosphere map total electron content (TEC), $E_{\rm X_AL}$, $E_{\rm X_ROC}$, and $E_{\rm X_JRO}$ on 19 March 2002. The upper panel represents the Latitude-LT-TEC plot at $-75^{\circ}\rm E$ longitude. Black dots are equatorial ionization anomaly crest locations. The lower panel displays the diurnal variation of $E_{\rm X_AL}$, $E_{\rm X_ROC}$, and $E_{\rm X_JRO}$. The magenta solid line is the average electric field in 300–400 km altitude at Jicamarca. The blue and black dotted lines are $E_{\rm X_AL}$ and $E_{\rm X_ROC}$, respectively, in the $-75^{\circ}\rm E$ longitude sector during 0900–1300 LT. The root-mean-square errors between $E_{\rm X_AL}$ and $E_{\rm X_ROC}$ as well as $E_{\rm X_AL}$ and $E_{\rm X_JRO}$ are 0.21 and 0.17 mV/m, respectively.

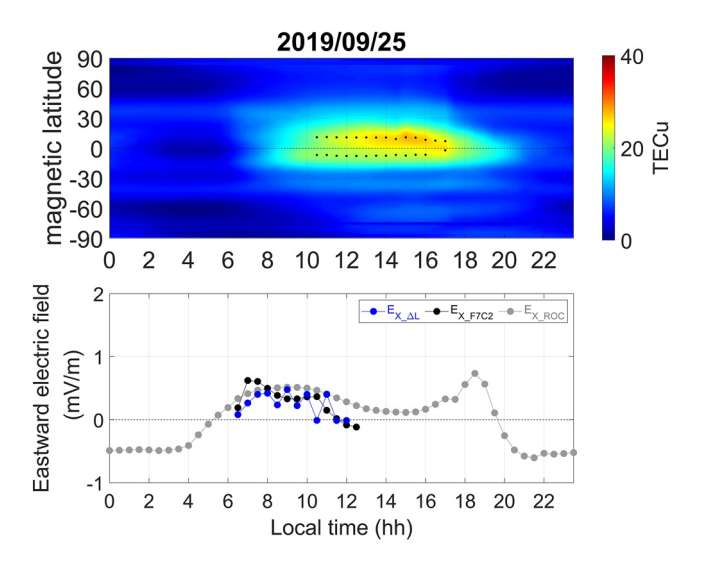


Figure 5. The diurnal variation of global ionosphere map total electron content (TEC), $E_{\rm X_AL}$, $E_{\rm X_F7C2}$, and $E_{\rm X_ROC}$ at $-120^{\circ}{\rm E}$ longitude on 25 September 2019. The upper panel represents the Latitude-LT-TEC plot at $-120^{\circ}{\rm E}$ longitude. Black dots are equatorial ionization anomaly crest locations. The lower panel displays the diurnal variation of $E_{\rm X_AL}$, $E_{\rm X_F7C2}$, and $E_{\rm X_ROC}$. The blue and black dotted lines are $E_{\rm X_AL}$ and $E_{\rm X_F7C2}$, respectively, in the $-120^{\circ}{\rm E}$ longitude sector during 0630–1230 LT. The gray dotted line is $E_{\rm X_ROC}$ shown in Figure 3. The root-mean-square errors between $E_{\rm X_AL}$ and $E_{\rm X_F7C2}$ as well as $E_{\rm X_AL}$ and $E_{\rm X_ROC}$ are 0.19 mV/m and 0.24 mV/m, respectively.

3. Results and Discussion

The GIM-TEC depicts that EIA crests of L_n and L_s move poleward and the distance between the two crests of ΔL becomes large when the associated equatorial eastward electric field derived by the ROCSAT-1 upward ion velocity is intense (Figure 2). The significant correlation coefficients of 0.62–0.89 between $\tilde{E}_{X \text{ ROC}}$ and $L_{\text{n}}/L_{\text{s}}/\Delta L$ in Figure 2 are in good agreement with previous studies (Chen et al., 2008; Rastogi & Klobuchar, 1990; Stolle et al., 2008). Figure 3 shows that the eastward electric field derived by GIM-TEC ΔL and that by the ROCSAT-1 database well agree with each other from 0400–0600 to 1200–1400 LT, which suggests that the crest distance, ΔL , in GIM-TEC can be an adequate proxy of the daily eastward dynamo electric field in the equatorial ionosphere. In general, $E_{\mathbf{X}_\Delta L}$ is more consistent with $E_{\rm X~ROC}$ during equinoxes than solstices due to the more prominent meridional wind effects during solstices (Khadka et al., 2018; Luan et al., 2015). Nonetheless, Table 1 shows that RMSEs are smaller than 0.3 mV/m in 26 out of 32 longitude regions. The discrepancies in Figure 3 are that $E_{\rm X~ROC}$ is smaller than $E_{X \Delta L}$ at -120° longitudes, where is the positive declination of the magnetic field, in J-month, as well as those at -30, 60, and 105° longitudes, where is the negative declination, in D-month. Note that Hartman and Heelis (2007) study measurements from the ion drift meter on the Defense Meteorological Satellite Program F15, and suggest that at the satellite altitude the meridional wind results in a westward dynamo electric field in the region where the declination is positive in J-month and negative in D-month. It might be the westward dynamo electric field suggested by Hartman and Heelis (2007) results in the smaller $E_{X \text{ ROC}}$ than the $E_{X \Delta L}$. Nevertheless, the discrepancies indicate that the meridional wind and declination are important at certain locations during certain seasons.

Over Jicamarca (-75° E longitude), $E_{\rm X_AL}$, $E_{\rm X_ROC}$, and $E_{\rm X_JRO}$ are generally in good agreements (RMSEs ranging from 0.10 to 0.13 mV/m), except that $E_{\rm X_JRO}$ is higher than $E_{\rm X_ROC}$ during 0400–0600 LT in J-month, which corresponds with the weaker correlation coefficient between the monthly averaged EEJ intensity and the monthly averaged EIA crest location in the American sector mainly in May-August as reported by Liu et al. (2020). On the other hand, the pattern of $E_{\rm X_AL}$ in -30° E longitude highly deviating from that of $E_{\rm X_ROC}$ in the 4 months might be due to limited available ground-based GNSS receiving stations in the region (see IGS, https://igs.org/network/#station-map-list), which results in less reliable acquisition of the EIA crest locations.

Figures 4 and 5 show that $E_{\rm X_\Delta L}$ agrees well with $E_{\rm X_ROC}$ and $E_{\rm X_F7C2}$ on individual days during the high and low solar activity periods, which demonstrate that $\Delta \rm L$ of GIM EIA crests can be employed to derive the eastward electric field of $E_{\rm X_\Delta L}$ daily. This is important that due to limited mission periods of satellite-based measurements and limited spatial coverage of the ground-based observations, one can take advantage of the GIM TEC to estimate the global daily dynamo electric fields. Meanwhile, Figure 6 shows the eastward electric field of $E_{\rm X_\Delta L}$ in various longitudes, seasons, and solar activities during 1999–2020. Li et al. (2017) examined the 11-year solar cycle response of the EIA observed by GPS radio occultation and found that during high solar activity periods, the location of the EIA crests moves ~10° poleward because of the enhanced E × B electromagnetic force. The agreements in the poleward motion of Figure 2 and Li et al. (2017) as well as in the solar activity effect of Figure 6 and Li et al. (2017) confirm that ΔL can be used to derive the daily eastward dynamo electric field. Several physical

CHENG ET AL. 6 of 10

slibrary wiley.com/doi/10.1029/2022SW003073 by University Of Colorado Librari, Wiley Online Library on [01/08/2023]. See the Terms

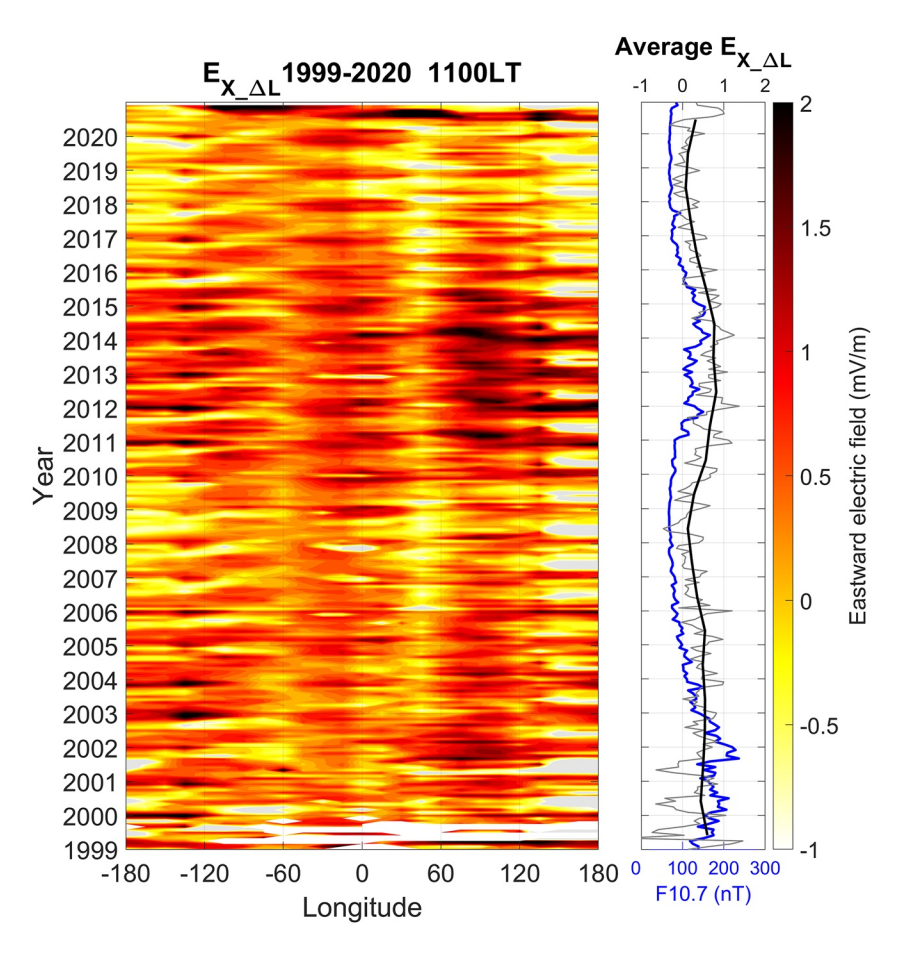


Figure 6. Annual variation of $E_{X_\Delta L}$ at 1100 LT in 1999–2020 (left) and the longitudinal average of the $E_{X_\Delta L}$ (right). The blue solid line is monthly F10.7, the gray solid line represents the longitudinal average of $E_{X_\Delta L}$ in various months, and the black solid line stands for the longitudinal average of $E_{X_\Delta L}$ in various years. Some data gaps might be due to the limited (about 70–130s) ground-based GNSS receivers available, which result in difficulties in identifying the equatorial ionization anomaly crest locations and in calculating the electric field in 1999.

based models of ionosphere, such as the SAMI-2/3 and the SUPIM utilize the empirical equatorial vertical drift model developed by Scherliess and Fejer (1999) and Fejer et al. (2008). It is found that these empirical vertical drift models are more realistic than the simplified sine function model representation of the vertical drift (Huba et al., 2000). Note that the abovementioned empirical models are constructed by using satellite and ground-based observations and the database has ended by 2004. Here, we employ the long-term observations of the CODE GIM EIA crests to derive the daily eastward dynamo electric field in 1999–2020, which covers two solar cycles with various solar activities.

Scientists investigate responses of dynamo electric fields and E \times B drifts to various ionospheric features, for example, large-scale tidal waves (Fang et al., 2009; Liu & Richmond, 2013) and irregularities (Basu et al., 2009; Huba et al., 2008), using various ionospheric physical models. To evaluate how the technique developed in this study improves the ionosphere models, $V_{Z_\Delta L}$ derived by $E_{X_\Delta L}$ and magnetic fields of IGRF via Equation 1 is further utilized as the input for the model runs of SAMI-2 at 60°E longitudes. Figure 7 displays an example outputs of the ionosphere model runs driven by the various vertical E \times B drifts at 3 September 2019. The simulations take vertical E \times B derived from Fejer-Scherliess empirical model, GIM-TEC $V_{Z_\Delta L}$ and ROCSAT-1 V_{Z_ROC} as input to the magnetic equator to drive the equatorial plasma fountain and EIA. As the vertical E \times B drifts from GIM-TEC is only available at 0430–1130 LT, we scale up/down the Fejer-Scherliess drifts of the entire day based on the percentage difference between the two models when GIM-TEC drifts are available to reconstruct the GIM-TEC derived drifts for the entire day. Figure 7a shows the three models of vertical E \times B drifts. TEC plots and their differences in Figure 7 are arranged in the global constant local time at 1400 LT in order to assess

CHENG ET AL. 7 of 10

15427390, 2022, 11, Downloaded from https://agupubs.onlinelibrary.wiley.com/doi/10.1029/2022SW003073 by University Of Colorado Librari, Wiley Online Library on [01/08/2023]. See the

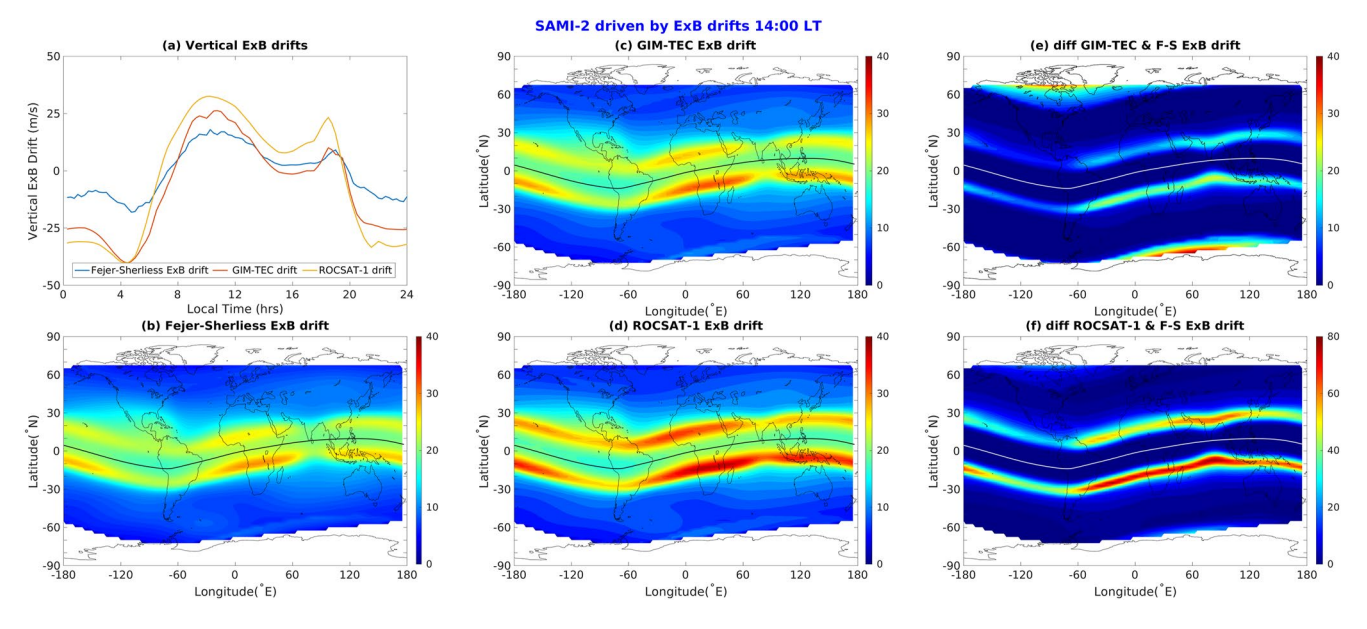


Figure 7. (a) Vertical $E \times B$ drifts from Fejer-Scherliess model (blue), global ionosphere map-total electron content (GIM-TEC) (red), ROCSAT-1 (orange) and (b–d) SAMI-2 model outputs driven by these $E \times B$ drifts at global constant local time of 1400 LT on 3 September 2019. Percentage differences of the model outputs in respect to the reference run of Fejer-Scherliess drift model are also plotted in (e) and (f). Black solid lines in (b–d) denote the magnetic equator of center-dipole coordinate used by SAMI-2. The root-mean-square error in (a) between $E \times B$ drifts from Fejer-Scherliess model and GIM-TEC is 12.09 m/s, and that between Fejer-Scherliess model and ROCSAT-1 is 16.26 m/s.

how the global ionosphere responses to the drift models. These simulation results show the corresponding EIA strengths in responses to the three drift models. Figure 7 confirms that our approach provides an alternative and novel way for deriving dynamo electric fields, which will continuously benefit the current ionosphere models for a better understanding of the ionospheric space weather during the various solar activity periods.

4. Conclusion

We confirm that ΔL in GIM TEC minimizing the trans-equatorial wind effects is a suitable proxy to derive the global eastward dynamo electric field in various longitudes, seasons, and solar activity levels. The values of our technique for the space weather application are summarized as follow:

- 1. One can evaluate the variations of vertical $E \times B$ drifts inferring from the same observation parameters (GIM-TEC). Whereas the vertical $E \times B$ drifts measured by difference instruments on board satellites may be suffered from the instrumental biases or uncertainties.
- 2. Routinely published GIMs allow us deriving the long-term dynamo electric field and the associated $E \times B$ drift across the globe. By contrast, ground-based radars and satellites usually yield limited spatial coverage and temporal resolution, respectively.
- Scientists can employ the developed model either as a stand-alone one to derive the electric field directly, or computing E x B drifts as input to the existing ionospheric model to have a better understanding on space weather.

Data Availability Statement

The authors gratefully acknowledge Taiwan Space Science Database for providing ROCSAT-1 data which can be obtained from https://cdaweb.gsfc.nasa.gov/pub/data/formosat-rocsat/formosat-1/, as well as NSPO and Taiwan Analysis Center for COSMIC for providing FORMOSAT-7/COSMIC-2 data. The total electron content (TEC) of global ionosphere maps is retrieved from the Center for Orbit Determination in Europe (https://cddis.nasa.gov/Data_and_Derived_Products/GNSS/atmospheric_products.html#iono). The Jicamarca incoherent scatter radar data can be obtained from the website of http://jro.igp.gob.pe/madrigal/.

CHENG ET AL. 8 of 10

15427390, 2022, 11, Downloaded

Acknowledgments

This work was financially supported by the Center for Astronautical Physics and Engineering from the Featured Area Research Center program within the framework of Higher Education Sprout Project by the Ministry of Education in Taiwan. This study is supported by the Ministry of Science and Technology (MOST) Grants MOST 109-2636-M-008-004 in Taiwan. SAMI-2 model code is from the open source code platform provide by Dr. Joseph Huba.

References

- Anderson, D. (1973). A theoretical study of the ionospheric F region equatorial anomaly-II. Results in the American and Asian sectors. *Planetary and Space Science*, 21(3), 421–442. https://doi.org/10.1016/0032-0633(73)90041-X
- Anderson, D., Anghel, A., Chau, J., & Veliz, O. (2004). Daytime vertical E × B drift velocities inferred from ground-based magnetometer observations at low latitudes. *Space Weather*, 2(11), S11001. https://doi.org/10.1029/2004SW000095
- Anderson, D., Anghel, A., Yumoto, K., Ishitsuka, M., & Kudeki, E. (2002). Estimating daytime vertical E × B drift velocities in the equatorial F-region using ground-based magnetometer observations. *Geophysical Research Letters*, 29(12), 1596. https://doi.org/10.1029/2001GL014562
- Bailey, G. J., & Balan, N. (1996). A low-latitude ionosphere-plasmasphere model. In R. W. Schunk (Ed.), *Solar-terrestrial energy program:* Handbook of ionospheric models.
- Bailey, G. J., Balan, N., & Su, Y. Z. (1997). The sheffield University plasmasphere model—A review. *Journal of Atmospheric and Solar-Terrestrial Physics*, 59(13), 1541–1552. https://doi.org/10.1016/S1364-6826(96)00155-1
- Basu, S. u., Basu, S., Huba, J., Krall, J., McDonald, S. E., Makela, J. J., et al. (2009). Day-to-day variability of the equatorial ionization anomaly and scintillations at dusk observed by GUVI and modeling by SAMI3. *Journal of Geophysical Research*, 114(A4), A04302. https://doi.org/10.1029/2008JA013899
- Bravo, M. A., Batista, I. S., Souza, J. R., & Foppiano, A. J. (2017). Equatorial ionospheric response to different estimated disturbed electric fields as investigated using Sheffield University Plasmasphere Ionosphere Model at INPE. *Journal of Geophysical Research: Space Physics*, 122(10), 10511–10527. https://doi.org/10.1002/2017JA024265
- Bravo, M. A., Batista, I. S., Souza, J. R., & Foppiano, A. J. (2019). Ionospheric response to disturbed winds during the 29 October 2003 geomagnetic storm in the Brazilian sector. *Journal of Geophysical Research: Space Physics*, 124(11), 9405–9419. https://doi.org/10.1029/2019JA027187
- Chang, Y.-S., Chiang, W.-L., Ying, S.-Y., Holt, B. J., Lippincott, C. R., & Hsieh, K.-C. (1999). System architecture of the IPEI payload on ROCSAT-1. Terrestrial, Atmospheric and Oceanic Sciences, 10(suppl), 7–18. https://doi.org/10.3319/TAO.1999.10.S.7(ROCSAT)
- Chen, C. H., Lin, C. H., Chang, L. C., Huba, J. D., Lin, J. T., Saito, A., & Liu, J. Y. (2013). Thermospheric tidal effects on the ionospheric midlat-itude summer nighttime anomaly using SAMI3 and TIEGCM. *Journal of Geophysical Research Space Physics*, 118(6), 3836–3845. https://doi.org/10.1002/jgra.50340
- Chen, C. H., Liu, J. Y., Yumoto, K., Lin, C. H., & Fang, T. W. (2008). Equatorial ionization anomaly of the total electron content and equatorial electrojet of ground-based geomagnetic field strength. *Journal of Atmospheric and Solar-Terrestrial Physics*, 70(17), 2172–2183. https://doi.org/10.1016/j.jastp.2008.09.021
- Dabas, R. S., Singh, L., Lakshmi, D. R., Subramanyam, P., Chopra, P., & Garg, S. C. (2003). Evolution and dynamics of equatorial plasma bubbles: Relationships to ExB drift, postsunset total electron content enhancements, and equatorial electrojet strength. *Radio Science*, 38(4), 1075, https://doi.org/10.1029/2001RS002586
- Davies, K. (1990). Ionospheric radio. Peter Peregrinus.
- Duncan, R. A. (1960). The equatorial F-region of the ionosphere. *Journal of Atmospheric and Terrestrial Physics*, 18(2–3), 89–100. https://doi.org/10.1016/0021-9169(60)90081-7
- Fang, T.-W., Kil, H., Millward, G., Richmond, A. D., Liu, J.-Y., & Oh, S.-J. (2009). Causal link of the wave-4 structures in plasma density and vertical plasma drift in the low-latitude ionosphere. *Journal of Geophysical Research*, 114(A10), A10315. https://doi.org/10.1029/2009JA014460
- Fang, T. W., Richmond, A. D., Liu, J. Y., & Maute, A. (2008). Wind dynamo effects on ground magnetic perturbations and vertical drifts. *Journal of Geophysical Research*, 113(A11), A11313. https://doi.org/10.1029/2008JA013513
- Fejer, B. G., Jensen, J. W., & Su, S. Y. (2008). Quiet time equatorial F region vertical plasma drift model derived from ROCSAT-1 observations. Journal of Geophysical Research, 113(A5), A05304. https://doi.org/10.1029/2007JA012801
- Fejer, B. G., Scherliess, L., & de Paula, E. R. (1999). Effects of the vertical plasma drift velocity on the generation and evolution of equatorial spread F. *Journal of Geophysical Research*, 104(A9), 19859–19869. https://doi.org/10.1029/1999JA900271
- Freeman, R. L. (2006). *Radio system design for telecommunication* (3rd ed.). Wiley-Interscience publication.
- Hanson, W. B., & Moffett, R. J. (1966). Ionization transport effects in the equatorial F region. *Journal of Geophysical Research*, 71(23), 5559–5572. https://doi.org/10.1029/IZ071i023p05559
- Harris, R. (2005). Radio communications in the digital age. Harris Corporation.
- Hartman, W. A., & Heelis, R. A. (2007). Longitudinal variations in the equatorial vertical drift in the topside ionosphere. *Journal of Geophysical Research*, 112(A3), A03305. https://doi.org/10.1029/2006JA011773
- Huba, J. D., Joyce, G., & Fedder, J. A. (2000). Sami2 is another model of the ionosphere (SAMI2): A new low-latitude ionosphere model. *Journal of Geophysical Research*, 105(A10), 23035–23053. https://doi.org/10.1029/2000JA000035
- Huba, J. D., Joyce, G., & Krall, J. (2008). Three-dimensional equatorial spread F modeling. Geophysical Research Letters, 35(10). https://doi.org/10.1029/2008GL033509
- Immel, T. J., Sagawa, E., England, S. L., Henderson, S. B., Hagan, M. E., Mende, S. B., et al. (2006). Control of equatorial ionospheric morphology by atmospheric tides. Geophysical Research Letters, 33(15), L15108. https://doi.org/10.1029/2006GL026161
- Kelley, M. C. (2009). The Earth's ionosphere: Plasma physics and electrodynamics (2nd ed.). Academic Press. 73.
- Khadka, S. M., Valladares, C. E., Sheehan, R., & Gerrard, A. J. (2018). Effects of electric field and neutral wind on the asymmetry of equatorial ionization anomaly. *Radio Science*, 53(5), 683–697. https://doi.org/10.1029/2017RS006428
- Klobuchar, J. A. (1991). Ionospheric effects on GPS. GPS World, 2(4), 48-51.
- Li, K.-F., Lin, L.-C., Bui, X.-H., & Liang, M.-C. (2017). The 11 year solar cycle response of the equatorial ionization anomaly observed by GPS radio occultation. *Journal of Geophysical Research: Space Physics*, 123(1), 848–861. https://doi.org/10.1002/2017JA024634
- Liu, H.-L., & Richmond, A. D. (2013). Attribution of ionospheric vertical plasma drift perturbations to large-scale waves and the dependence on solar activity. *Journal of Geophysical Research: Space Physics*, 118(5), 2452–2465. https://doi.org/10.1002/jgra.50265
- Liu, J., Zhang, D., Mo, X., Xiong, C., Hao, Y., & Xiao, Z. (2020). Morphological differences of the northern equatorial ionization anomaly between the eastern Asian and American sectors. *Journal of Geophysical Research: Space Physics*, 125(3), e2019JA027506. https://doi. org/10.1029/2019JA027506
- Luan, X., Wang, P., Dou, X., & Liu, Y. C.-M. (2015). Interhemispheric asymmetry of the equatorial ionization anomaly in solstices observed by COSMIC during 2007–2012. *Journal of Geophysical Research: Space Physics*, 125(4), 3059–3073. https://doi.org/10.1002/2014JA0208
- Rastogi, R. G., & Klobuchar, J. A. (1990). Ionospheric electron content within the equatorial F2 layer anomaly belt. *Journal of Geophysical Research*, 95(A11), 19045–19052. https://doi.org/10.1029/JA095iA11p19045
- Ratcliffe, J. A. (1974). An introduction to the ionosphere and the magnetosphere. Web.
- Roy, B., DasGupta, A., & Paul, A. (2013). Impact of space weather events on satellite-based navigation. Space Weather, 11(12), 680–686. https://doi.org/10.1002/2013SW001001

CHENG ET AL. 9 of 10

- Sagawa, E., Immel, T. J., Frey, H. U., & Mende, S. B. (2005). Longitudinal structure of the equatorial anomaly in the nighttime ionosphere observed by IMAGE/FUV (2005). *Journal of Geophysical Research*, 110(A11), A11302. https://doi.org/10.1029/2004JA010848
- Scherliess, L., & Fejer, B. G. (1999). Radar and satellite global equatorial F region vertical drift model. *Journal of Geophysical Research*, 104(A4), 6829–6842. https://doi.org/10.1029/1999JA900025
- Stolle, C., Manoj, C., Lu'hr, H., Maus, S., & Alken, P. (2008). Estimating the daytime Equatorial Ionization Anomaly strength from electric field proxies. *Journal of Geophysical Research*, 113(A9), A09310. https://doi.org/10.1029/2007JA012781
- Su, S.-Y., Yeh, H. C., Heelis, R. A., Wu, J. M., Yang, S. C., Lee, L. F., & Chen, H. L. (1999). The ROCSAT-1 IPEI preliminary results: Low latitude ionospheric plasma and flow variations. *Terrestrial, Atmospheric and Oceanic Sciences*, 10(4), 787–804. https://doi.org/10.3319/TAO.1999.10.4.787(ROCSAT)
- Wright, J. W. (1963). The F-region seasonal anomaly. Journal of Geophysical Research, 68, 4379–4381. https://doi.org/10.1029/JZ068i014p04379
 Yeh, H. C., Su, S.-Y., Heelis, R. A., & Wu, J. M. (1999). The ROCSAT-1 IPEI preliminary results: Vertical ion drift statistics. Terrestrial, Atmospheric and Oceanic Sciences, 10(4), 805–820. https://doi.org/10.3319/Tao.1999.10.4.805(Rocsat
- Yeh, K. C., Flaherty, B. J., & Bolfing, B. J. (1972). A study of the dependence of the maximum useable frequency on the electron content. Proceedings of the IEEE, 60(9), 1099–1100. https://doi.org/10.1109/PROC.1972.8856
- Yue, X., Schreiner, W. S., Pedatella, N. M., & Kuo, Y.-H. (2016). Characterizing GPSradio occultation loss of lock due toionospheric weather. Space Weather, 14(4), 285–299. https://doi.org/10.1002/2015SW001340

CHENG ET AL. 10 of 10